

Chapter 2

First order Smectic A-Smectic C*/ Smectic A-Smectic C transition

2.1 Introduction

Recently, there has been considerable interest in the theoretical and experimental studies of first order phase transitions. The field of second order transitions and associated critical phenomena has advanced enormously as compared to that of first order transitions. One of the major difficulties associated with the first order transitions is that they can not be, unlike second order ones, classified into universality classes. The reason is that at a second order transition the correlation length diverges and becomes much larger compared to any system-specific lengths for e.g., molecular length. Hence short wave length properties of the system become irrelevant as far as the critical behaviour is concerned. However, there is no such microscopic length associated with a first order transition and as a consequence much less universality is expected in the case of such a first order transition. But first order transitions are important because of some unique problems associated with these transitions, for example, nucleation, spinodal decomposition, finite size effects etc. ~ Therefore, observation of a first order transition in any new condensed matter system would help in getting a better insight into these problems. Some well known examples of first order transitions are liquid - gas, liquid - solid, ferromagnetic - antiferromagnetic, smectic A - nematic (A-N) phase transitions etc. In this chapter, we present the experimental results on a liquid crystalline system which led to the first unambiguous observation of such a transition between smectic A and smectic C* phases.

The scheme of presentation in this chapter is as follows: first a brief introduction to phase transitions which includes the basic thermodynamic classification

of the order of the transition and also about the concept of the order parameter. Next we summarise the earlier theoretical and experimental studies on the nature of the smectic A-smectic C (A - C) and the smectic A-smectic C* transitions. After this a detailed description of the X-ray set up, used for the studies described in this chapter as well as for most of the studies described in the subsequent chapters, is given. This is followed by our experimental results which describe the observation of a first order A-C* transition and finally a discussion regarding the origin of the first order nature of the A-C or A-C* transition.

A phase transition occurs when the state of the system must change to achieve equilibrium. The Ehrenfest classification of phase transitions is based on the behaviour of the derivatives of the free energy F with respect to parameters like for example temperature. If the phase transition is accompanied by any of the first derivatives of F exhibiting a jump, (e.g., volume, enthalpy) then the transition is classified as first order type. If the first derivatives are continuous but second derivatives like for e.g., heat capacity, thermal expansivity etc., are singular then it is referred to as a second order transition. A first order transition involving discontinuous change in enthalpy is represented graphically in Figure 2.1(a). Curves H_I, H_{II} represent the variations in the enthalpies of phases I and II at constant pressure. In Figure 2.1(b) variations of enthalpy as a function of temperature for a second order transition is shown. (The first order transition is also known as discontinuous transition. The second order transition is generally referred as continuous, because higher order transitions are rare compared to first and second order ones. In this scheme, after Landau[1], the symmetry change across the transition plays a very important role in deciding the nature

Chapter 2: First order A-C / A-C* Transition

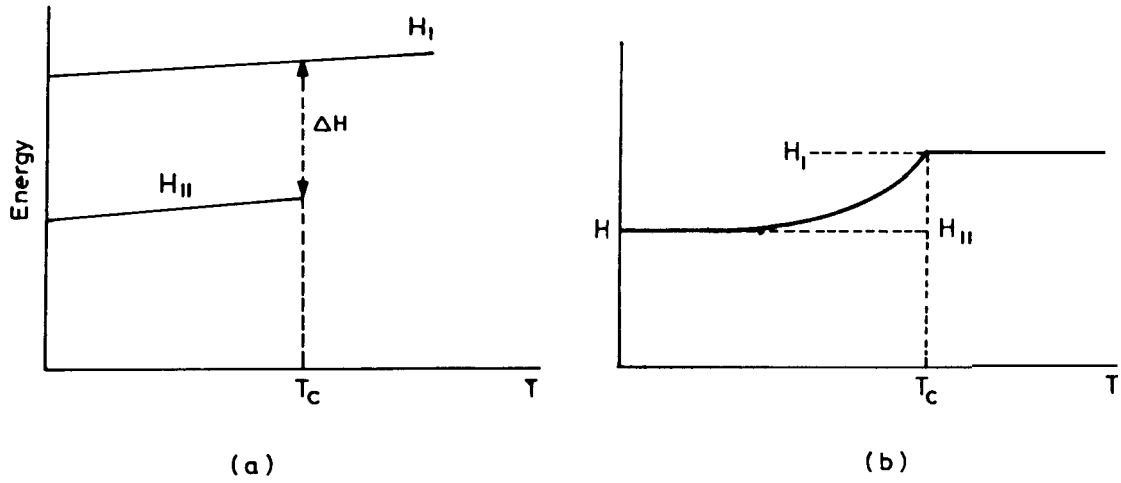


Figure 2.1: (a) A graphical representation of a first order transition involving discontinuous change in enthalpy. H_I and H_{II} represent the variation in enthalpies respectively of phases I and II at constant pressure. (b) Variation of enthalpy as a function of temperature for a second order transition.

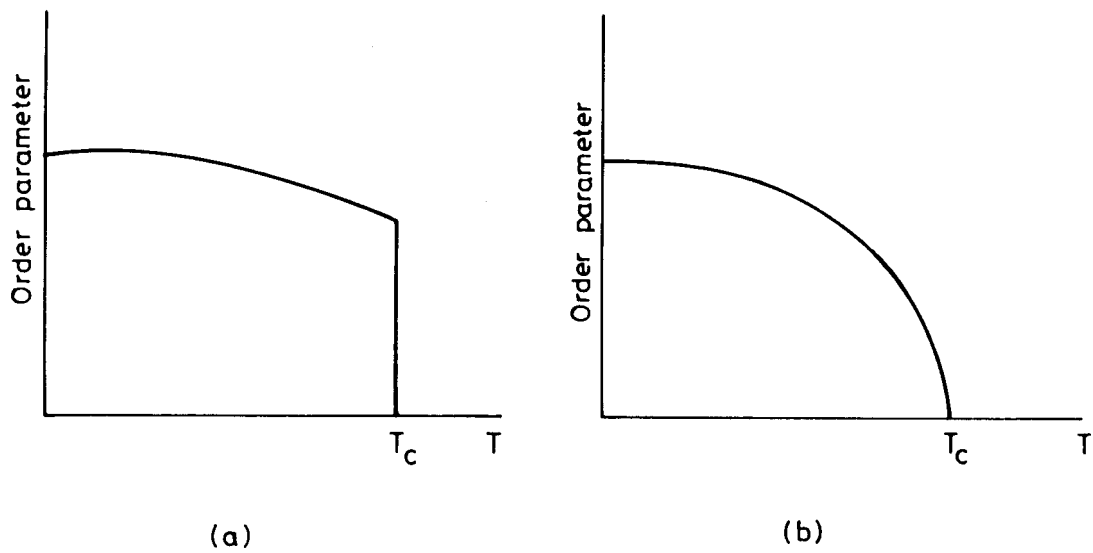


Figure 2.2: Variation of order parameter as a function of temperature for (a) first order transition. (b) second order transition

Chapter 2: First order A-C* / A-C Transition

of the transition.)

To describe quantitatively the change in the microscopic structure of the system when it passes through a phase transition, a quantity called 'order parameter' is defined in such a way that it takes a nonzero value in the unsymmetrical (or ordered) phase and is zero in the symmetrical phase (or disordered phase)[1]. For e.g., the order parameter for the ferromagnetic - paramagnetic transition is the spontaneous magnetization. Based on Landau's classification[1], at the onset of a first order transition the order parameter changes discontinuously, while at a second order transition it varies continuously. Figures 2.2(a) and 2.2(b) show the variation of the order parameter as a function of temperature for a first order and a second order transitions respectively.

2.1.1 Smectic A-Smectic C/Smectic A-Smectic C* transition

As we have already seen in Chapter 1, smectic A(A) and smectic C(C) phases are described as orientationally ordered fluids with a one dimensional mass density wave. In the A phase, the wave vector of the mass density wave is along the director and in the C phase it is at an angle. If the molecules are optically active[2] in the C phase, then it is known as smectic C* (C*) or chiral C phase. In the C* phase, the molecules are not only tilted with respect to the layer normal but the azimuthal direction of the tilt precesses from one layer to another, giving rise to a helicoidal structure. Due to the chirality of the molecules, the tilt ordering locally breaks the axial symmetry around the long molecular axis and induces a transverse in-plane polarisation. Thus a chiral C phase shows

ferroelectric properties[3] i.e., it has a nonzero spontaneous polarisation (P_s) when the helix is unwound.

The order parameter for the A-C transition is a complex one[4] and can be written as

$$\psi = \theta e^{i\phi}$$

where θ is the magnitude of the tilt angle and ϕ , the azimuthal angle (see Figure 2.3). Since ϕ can be chosen arbitrarily, θ itself is taken as the order parameter in the free energy expansion for the A-C transition. In the case of A-C* transition, in addition to tilt, spontaneous polarisation (P_s) is also present and one should, in principle, consider both the order parameters. But experimental evidence[5] indicates that the transition is brought about by the same intermolecular forces producing the C phase and not by a ferroelectric coupling between the permanent dipoles. Therefore, P_s becomes a secondary order parameter for the A-C* transition, whereas tilt angle θ is the primary order parameter. Thus the basic physics of the A-C* transition may be expected to be the same as that of A-C transition.

From symmetry considerations, A-C/A-C* transitions can either be first order or second order. But experimentally, this transition was generally found to be second order. Lien and Huang[6] predicted that the transition can be driven to become first order by large fluctuations of a nearby A-Isotropic transition. However, the existence of a first order A-C/A-C* transition had not been established experimentally so far. A significant advance in this direction was due to the synthesis[7,8] of many new ferroelectric liquid crystals which showed a high

Chapter 2: First order A-C / A-C* Transition

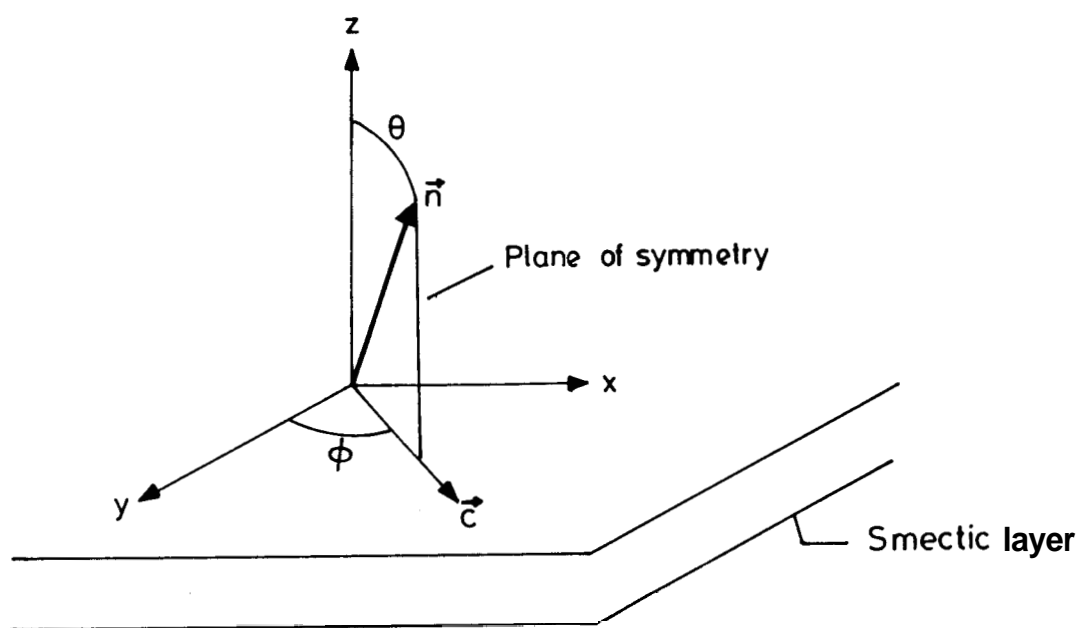


Figure 2.3: Geometry of smectic C phase.

value of spontaneous polarisation. Preliminary X-ray, spontaneous polarisation and differential scanning calorimetric (DSC) studies [7,9] had indicated that the A-C* transitions in some of these materials may be first order. We undertook high precision X-ray studies on one such ferroelectric material which has a high P_S (~ 300 nC/cm²). The results clearly showed that the A-C* transition in this material is first order. In order to understand the origin of the first order transition in such materials, X-ray diffraction experiments were carried out on two more liquid crystalline systems, the results of which are also described in the following sections.

2.2 Experimental

2.2.1 Materials used

The materials used for the studies described in this chapter are 4- (3-methyl -2- chloropentanoxy) -4' -heptyloxy biphenyl (MCP7OB), 4- (3-methyl -2- chloro butanoxy) -4' -heptyloxy biphenyl (A7 [left-handed] or A7[l]) and the terephthal -bis -alkylaniline (TBnA) series. The structural formulae and the transition temperatures of the materials are tabulated in Tables 2.1(a) and 2.1(b).

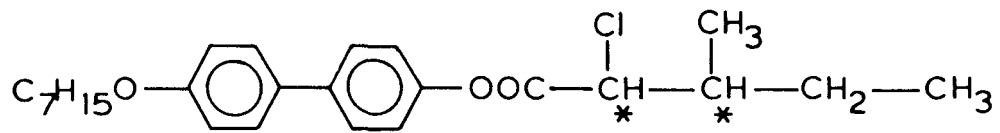
2.2.2 X-ray diffractometer set up

We describe here two types of X-ray diffractometer set up, one with a scintillation counter as the detector and another with a position sensitive detector.

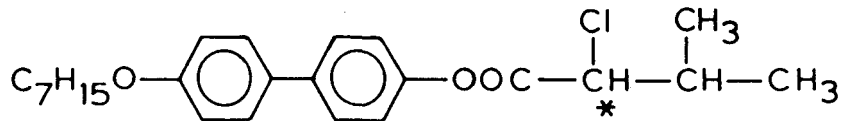
Chapter 2: First order A-C* / A-C transition

Table 2.1: (a)Structural formuale and transition temperatures (°C) of MCP7OB and A7[l]

MCP7OB



A7

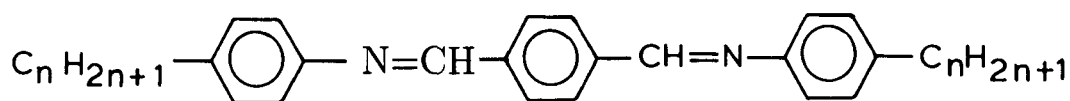


Material	Iso	A	C*	G*
MCP7OB	. 63	. 54	. 42.2	.
A7[l]	. 1	. 73.3	. 71.0	.

Chapter 2: First order A-C* / A-C transition

Table 2.1: (b)Structural formula and transition temperatures (°C) of TBnA series

TBnA



Material	Iso	A	C	I	F
TBDA	. 191.0	. 189.2	. 154.8	. 148.7	.
TBOA	. 202.5	. 192.5	. -	. 156.5	.
10 mol% TBOA+TBDA	. 191.6	. 188.7	. 153.5	. 148.9	.

Iso = isotropic phase, N = nematic, A = smectic A

C = smectic C, C* = chiral smectic C

G* = chiral smectic G phase, I = smectic I phase.

2.2.3 Scintillation counter set up

Since this set up was used for most of our experiments we shall describe it in greater detail.

A conventional X-ray generator (Enraf Nonius, model 583) with a fine focus tube (Philips PW 2213/20 copper anode) was used. The maximum operating conditions of the tube were 50 kV and 26 mA. But, generally it was operated at 40 kV and 26 mA, because it was found that increasing the operating voltage beyond 40 kV increases the background radiation and does not really help in getting better X-ray data. The monochromator input slits were kept wide open to avoid spurious trimming of the incoming beam. A bent quartz crystal monochromator cut for (1011) reflections was used in the Johansson geometry. The crystal was oriented to select the characteristic $\text{CuK}\alpha$ radiations. The monochromator intermediate slits are further trimmed to eliminate the $\text{K}\alpha_2$ rays so that the highly monochromatic $\text{K}\alpha_1$ ($\lambda = 1.54051$) rays emerge from the output slit of the monochromator. These rays get focussed on the circumference of the Guinier circle. The detector, viz., a NaI scintillation counter (Bicron) was placed on the circumference of the Guinier circle and the asymmetric transmission mode was used. A platinum edged slit, which was razor sharp - to eliminate any shadow effects - was used to control the width of the beam falling on the counter. The vertical divergence of the scattered beam was controlled by a pair of sller slits located in front of the detector. To avoid the direct beam falling on the detector, a beam stopper was suitably positioned. The Figure 2.4 shows a schematic view of the scattering geometry used in the experiments.

Chapter 2: First order A-C / A-C* Transition

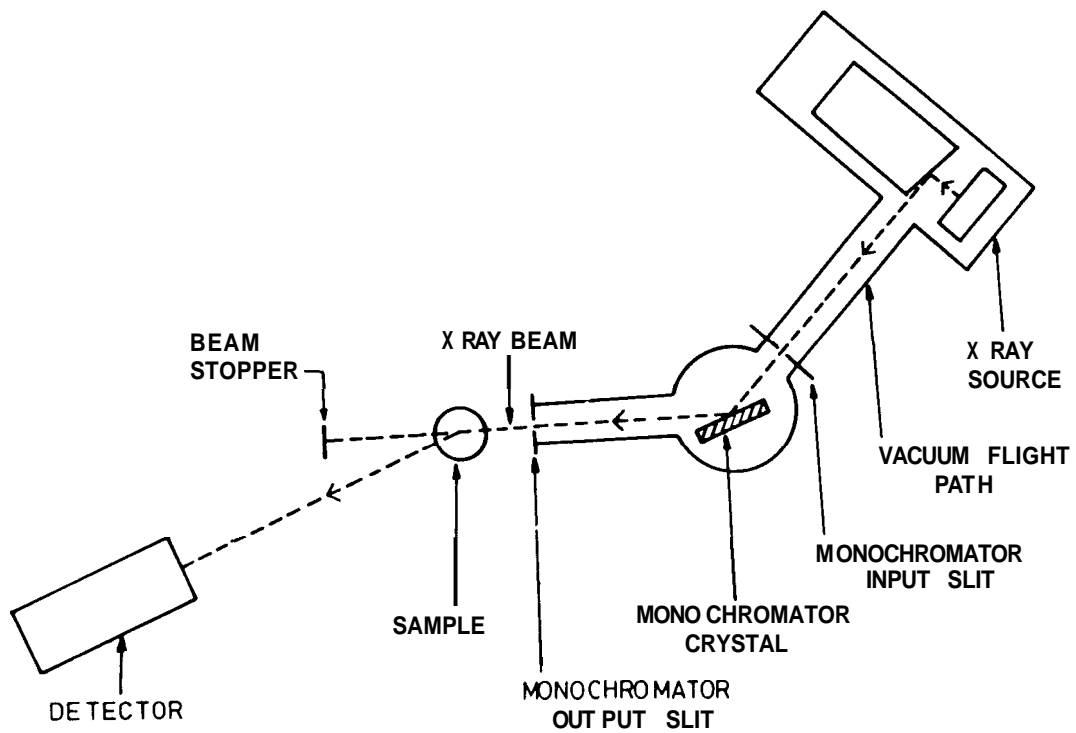


Figure 2.4: Schematic representation of the scattering geometry used in the X-ray set up. The detector is either a scintillation counter or a position sensitive detector depending on the set up used.

Chapter 2: First order A-C* / A-C Transition

Sample holder and heater design

The design of the sample holder and the heater was essentially the same as the one described by Somashekara[10] except for a few modifications. Schematic diagram of the sample holder is shown in Figure 2.5(a). It was made of a copper rod. A narrow capillary bore was drilled along the axis of the rod from top end to house the Lindemann capillary which contains liquid crystalline samples. The bore was about 0.9 mm in diameter and 20mm long. A pair of slots were cut on the rod along the length diametrically opposite to each other. These slots serve as the entrance and exit slits for the X-ray beam. The exit slot has its edges tapered to give an angle of 20° at the axis of the cylinder. The stem of the sample holder helps in fixing it on to the goniometer base.

Figure 2.5(b) shows the sectional view of the heater assembly. Essentially, it is a thicker copper rod, having a cavity, cut along the axis to house the sample holder. Two vertical slots cut on the cylinder serve as the entrance and exit windows for the X-ray beam. One of the junctions of the chromel-alumel thermocouple sheathed in a ceramic tube is fixed on the top end of the copper rod in such a way that the tip of the junction sits in close proximity to the sample in the sample holder. The temperature of the sample was varied by regulating the current passed through the thermfoil (MINCO) heater wrapped around the copper rod. The thermfoil was covered by two layers of thermal insulation composed of asbestos and hylam cylinders. This greatly reduces the heat loss due to radiation. The entrance and exit windows on the cylinder are covered using thin mylar sheets to prevent the air draughts. A guide screw

Chapter 2: First order A-C / A-C* Transition

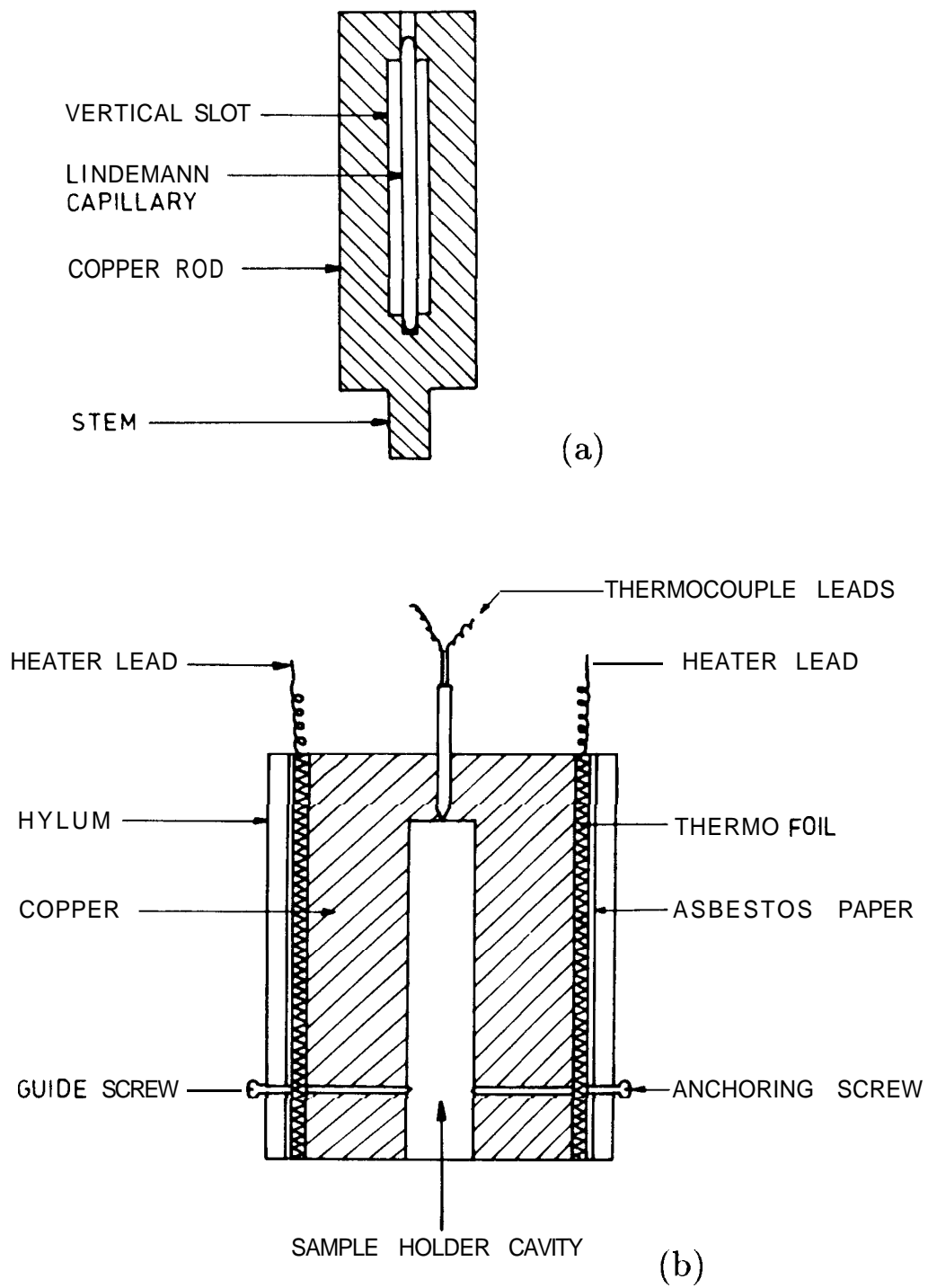


Figure 2.5: A cross-sectional view of (a) the sample holder, (b) the heater assembly

helps the sample holder windows to align properly with those of the heater. An anchoring screw was used in order to hold the sample holder firmly on to the body of the heater. The entire set up was housed in a chamber covered with thermal insulating sheets.

Temperature calibration

In order to obtain the true sample temperatures, the thermocouple was calibrated using standard substances exhibiting very sharp phase transitions. A laser transmission technique was used to determine the transition temperatures of the samples. The laser beam transmitted through the sample was collected by a photodetector, the output of which was recorded on a multichannel recorder. The thermocouple output (in mV) was read by a high resolution and low drift voltmeter (Keithley nanovoltmeter model 181) and was also monitored continuously using another channel of the same recorder. The criterion used in selecting the samples was that they exhibit strong and sharp intensity changes across the phase transitions. The sharp change in the intensity at a phase transition was recorded by the chart recorder and the corresponding thermo emf (in mV) was measured. The true transition temperatures of the samples were determined using a programmable, calibrated hot stage (Mettler FP 82). Transition temperatures in °C and the thermo emf in mV for various samples are tabulated in Table 2.2. The thermo emf vs the temperature data can be described by a polynomial[11]. We have fitted the data to a fifth degree polynomial, $T = a_0 + a_1V + a_2V^2 + a_3V^3 + a_4V^4 + a_5V^5$, where a_0, a_1, a_2, a_3, a_4 and a_5 are the constants and V is the thermoemf in millivolts. The Figure 2.6 shows the

Chapter 2: First order A-C* / A-C transition

Table 2.2: Thermocouple calibration of the heater. Materials used and the transition temperatures.

Compound	Transition Temp (°C) (Mettler)	Thermo emf (mV) (heater)	Fit values
8CB	40.5	1.5577	40.50
SOCB	80.7	3.2018	80.60
8S5	86.50	3.4458	86.50
CBOOA	107.9	4.3410	107.85
PAP	167.7	6.8446	167.70
p-anisaldazine	183.7	7.4972	183.65

Chapter 2: First order A-C / A-C* Transition

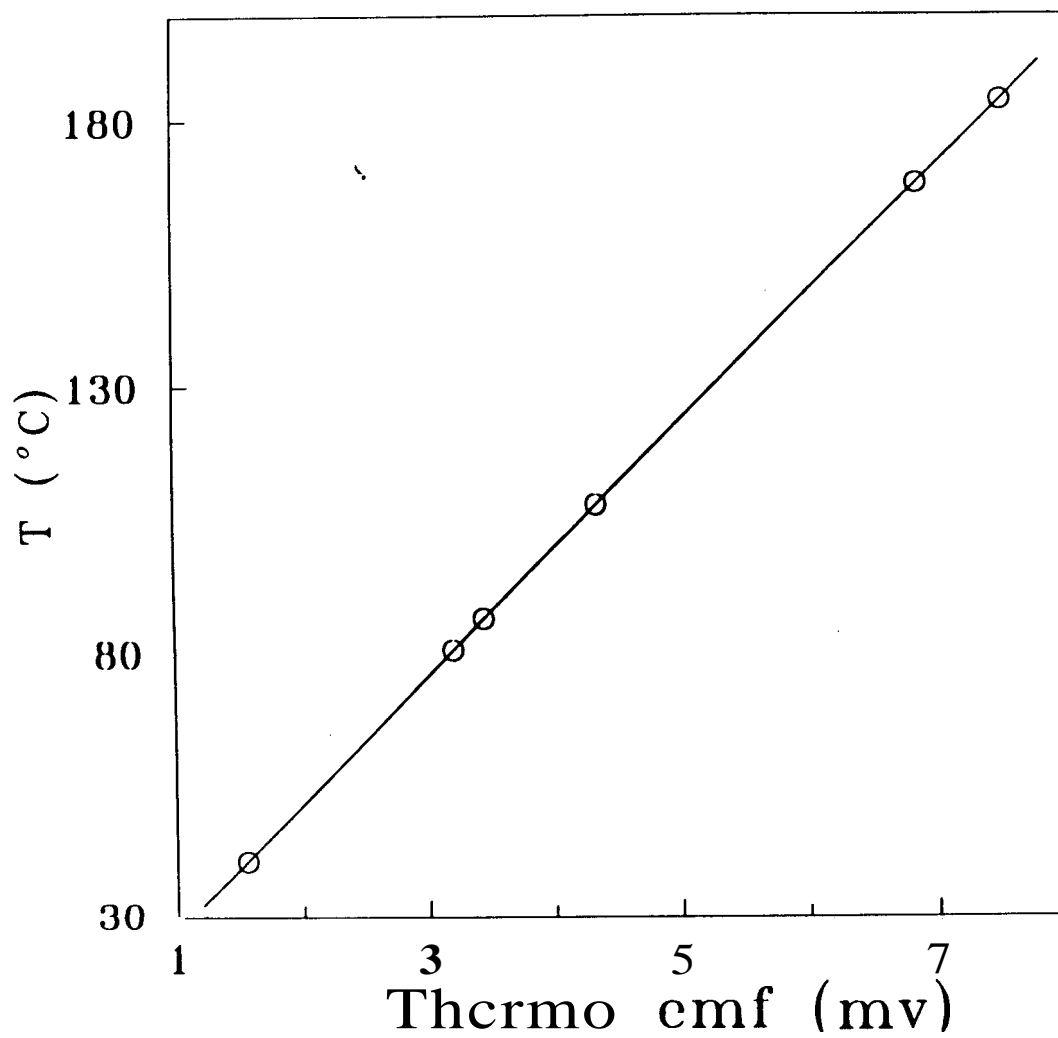


Figure 2.6: Temperature calibration curve for the X-ray heater. The straight line is a fit to a 5th degree polynomial.

the polynomial fit to the data. It can be seen from the figure that the polynomial fits the data extremely well and can be satisfactorily used to convert the thermocouple output to sample temperature.

Measuring Electronics

The X-ray beam impinges on the NaI crystal of the scintillation counter, and the output obtained is in the visible region. This was detected by a photomultiplier, the output of which was amplified in two stages. One by a preamplifier module and another by a high fidelity wide band amplifier. The amplified signal was discriminated by a pulse height discriminator circuit, which was made to operate in the optimum gain and plateau output region. The output of this unit was taken to a ratemeter which serves as an analogue indicator of the magnitude of the X-ray intensity falling on the detector. A parallel output of the discriminator was fed into an impulse counter which gives the output in terms of counts per unit time. The position of the detector, mounted on an arm (which moves along the Guinier circle) was controlled by a stepper motor and worm gear assembly. The stepper motor in turn was driven by a commercially available stepper motor control unit (Huber SMC 9002). The stepper motor control provided an overall angular resolution of 0.001° in Bragg angle. The impulse counter mentioned above was also built into this unit. Both these angular positioning and intensity measuring units were independently monitored and controlled by a micro computer (HP86B) using a serial interface. In addition to this, the temperature reading voltmeter was also interfaced to the computer. The entire operation of positioning the detector, measuring the intensity and the sample tempera-

ture were completely automated by writing a software program in BASIC. The online microcomputer was used not only for collection and storage of the data but also for preliminary analyses of the data. Figure 2.7 shows the schematic representation of the experimental set up.

A brief account of a typical X-ray experiment is given below.

The liquid crystal sample was filled in a Lindemann capillary (0.7 mm diameter, 17-20 mm length) in the isotropic or nematic state using a microsyringe with fine control. The length of the sample taken was usually about 10 mm. Sufficient gaps were left on either sides of the sample, so that when both the ends of capillary were sealed using a thin flame, the sample was not overheated. The capillary was then inserted into the cavity of the sample holder. This in turn was mounted inside the heater. The entrance and exit windows of the holder were aligned properly with that of the heater using the guiding screw. With the help of the anchoring screw, the holder was fixed firmly inside the heater. The heater was kept in between the pole pieces of a 2.4 T magnetic field generated by an electromagnet (Bruker B-E 25). The sample was heated to the isotropic or nematic phase and then cooled slowly (1-2°C/hour) to the A phase in the presence of the field. After obtaining a well aligned A phase, the sample along with the temperature controlled oven was transferred to the goniometer head of the diffractometer. An initial scan was taken in the equatorial direction by changing the position of the counter in steps of 0.01°. This gives an approximate position of Bragg angle Θ . A refined Θ scan was taken around this Θ position by varying the counter position in steps of 0.001°. The data was fitted to a

Chapter 2: First order A-C / A-C* Transition

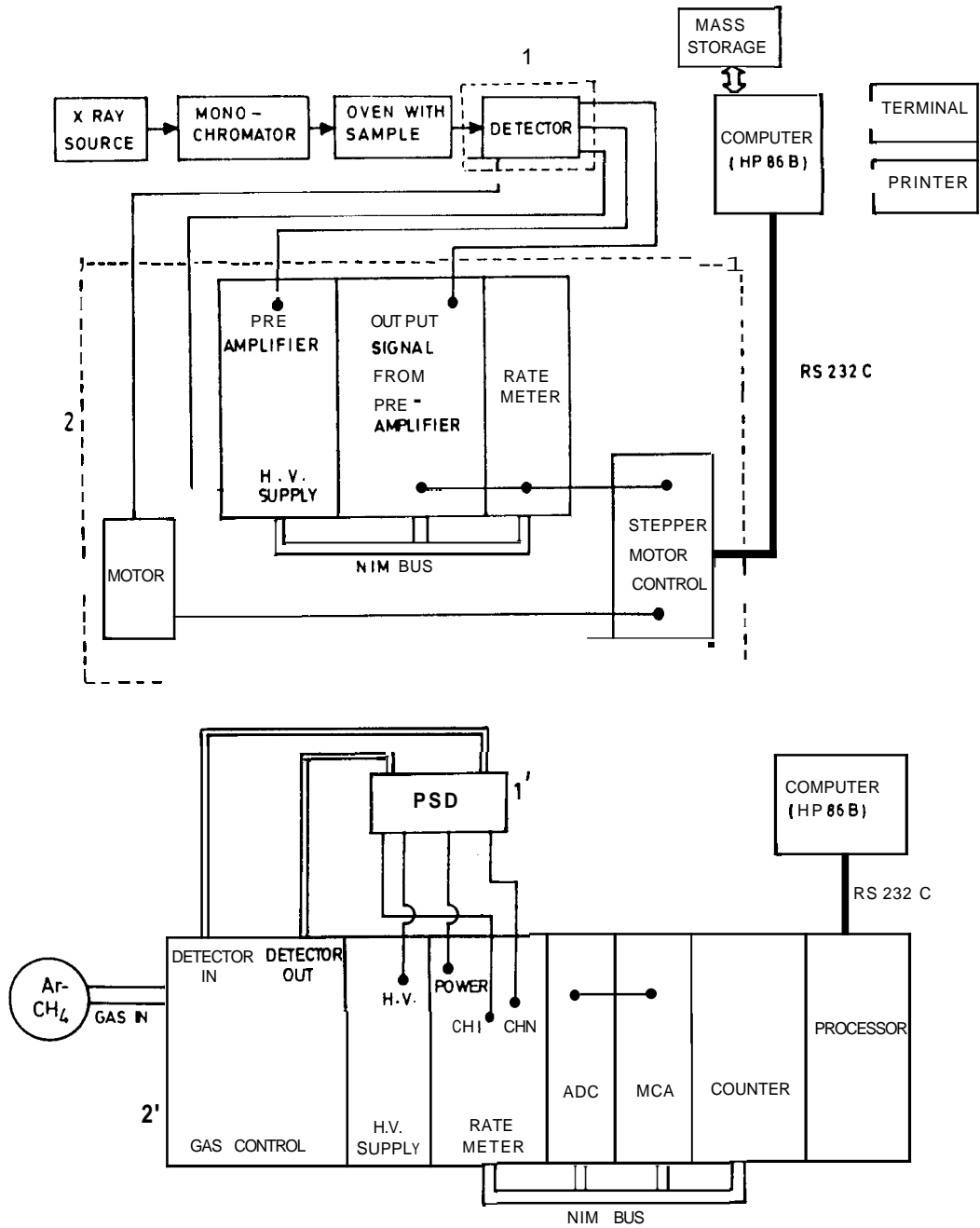


Figure 2.7: Block diagram of the experimental set up. 1.Scintillation counter. 1' position sensitive detector. 2 Single channel analyser set up. 2' Multichannel analyser set up.

second degree polynomial using least-squares-fit programme to give the peak Θ value and also the peak intensity. The value was corrected using the wave vector calibration value (discussed in 52.2.6). This was used for calculating the layer spacing (d) value,

$$d = \frac{\lambda}{2 \sin \Theta} \quad (2.1)$$

A typical X-ray scan is shown in Figure 2.8. The tilt angle in the C or C* phase was calculated by using the relation

$$\theta = \cos^{-1} \left(\frac{d_{C^*}}{d_A} \right) \quad (2.2)$$

where d_{C^*} and d_A are the layerspacing in C* and A phases respectively.

Wave vector calibration

The layerspacing (d) measured as described above may vary from the true value due to the limitations of the experimental set up. In order to account for this we have measured the scattering angle Θ for a set of standard compounds exhibiting A phase for which the true scattering angles (Θ') are known [12,13]. The deviation of the measured angle ($\Delta\theta = \Theta' - \Theta$) from the true value was calculated in each case and the correction to any subsequent measured Θ was calculated using the standard interpolation technique. The materials chosen for calibration, the standard scattering angle Θ' from known layerspacing, Θ , the scattering angle measured using our experimental set up and $\Delta\theta$ are listed in Table 2.3.

Chapter 2: ~~First~~ order A-C / A-C* Transition

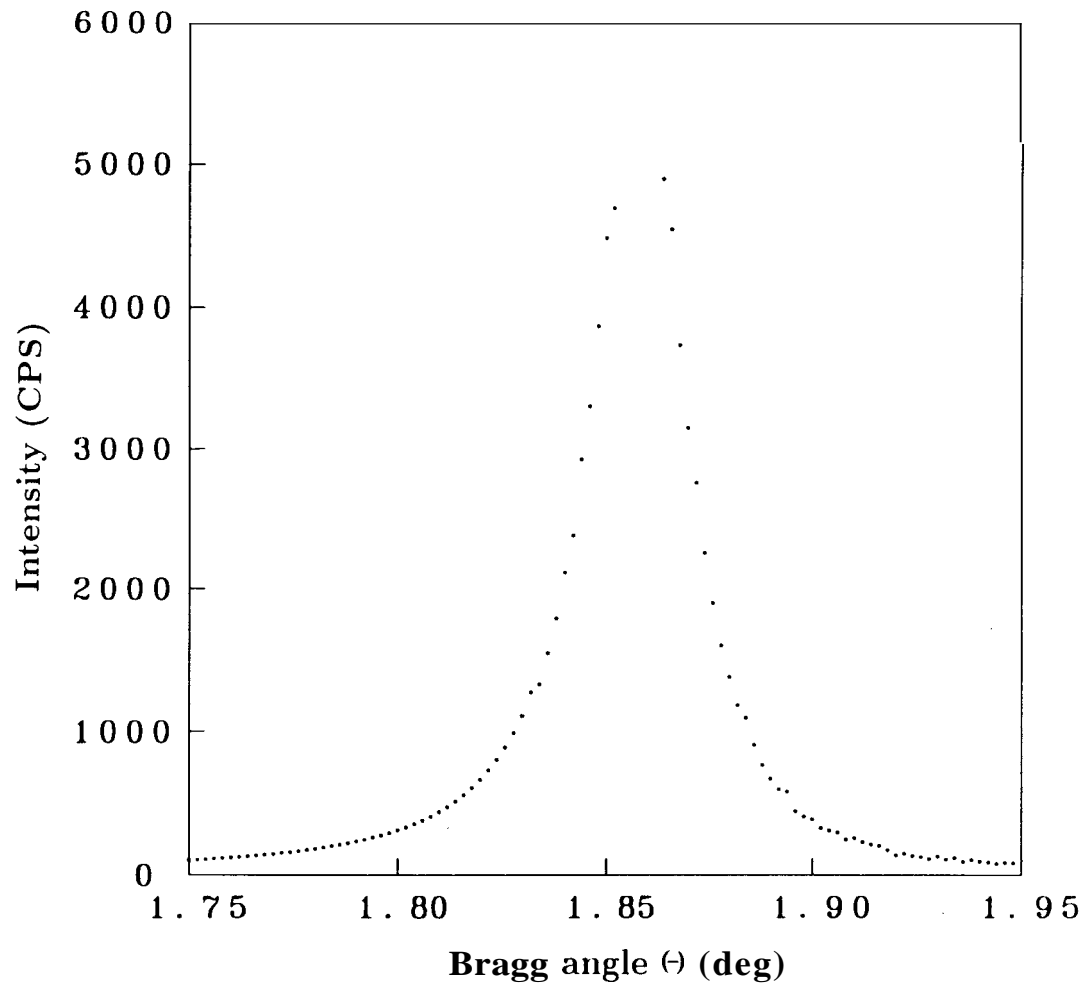


Figure 2.8: A typical X-ray scan taken along the equatorial direction

Chapter 2: First order A-C* / A-C transition

Table 2.3: Wave vector calibration.

Compound	Standard Θ' (deg)	Measured Θ (deg)	$\Delta\Theta = \Theta' - \Theta$ (deg)
CBOOA	1.2574 ¹²	1.1867	0.0707
DB5	1.7354 ¹³	1.6602	0.0752
8OCB	1.3838 ¹²	1.3122	0.0716

Chapter 2: First order A-C* / A-C Transition

Wave vector resolution

Even at the smallest slit width permitted by the set up ($10\mu\text{m}$), the intensity-scattering angle ($I-\Theta$) scan shows a peak with half width at half maximum of $d\theta = 0.01^\circ$. The wave vector spread or the resolution (dq) in the equatorial direction calculated from the equation, $dq = \frac{4\pi}{\lambda} \cos \Theta d\Theta$, for a typical scattering angle of 1.1° , was $1.42 \times 10^{-3} \text{ \AA}^{-1}$. The precision in determination of q itself at any temperature was $2 \times 10^{-4} \text{ \AA}^{-1}$.

2.2.4 Position sensitive detector set up

A Ge monochromator (having a much larger focal length than quartz) instead of the quartz monochromator and a linear position sensitive detector (PSD-Braun OED 50) in conjunction with a multichannel analyses (Braun MCA 3/1) in place of a scintillation counter are used in this set up.

The experiments were conducted using an aligned A phase obtained by cooling the sample at a slow rate ($-1^\circ\text{C}/\text{hour}$) from the isotropic phase in the presence of an *insitu* 0.8T magnetic field provided by a pair of samarium cobalt magnet pieces. The precision in determination of the wave vector was $2 \times 10^{-4} \text{ \AA}^{-1}$ while the resolution in the equatorial direction is $1 \times 10^{-3} \text{ \AA}^{-1}$ half width at half maximum (HWHM).

2.3 Results and Discussion

Figure 2.9 shows the differential scanning calorimetric (Perkin-Elmer DSC- TADS 4) scan taken for MCP7OB at a cooling rate of $1^\circ\text{C}/\text{min}$. The scan shows a

Chapter 2: First order A-C / A-C* Transition

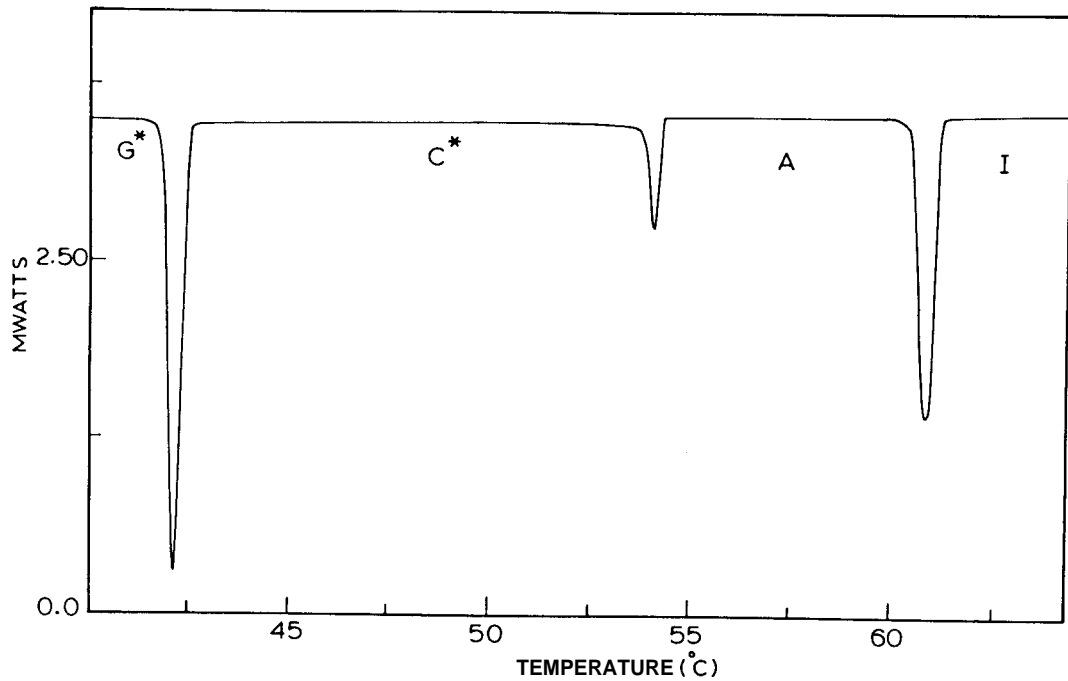


Figure 2.9: The differential scanning calorimetric scan taken for MCP70B at a rate 2° C /min in the cooling cycle. A strong peak for the A - C* transition is seen.

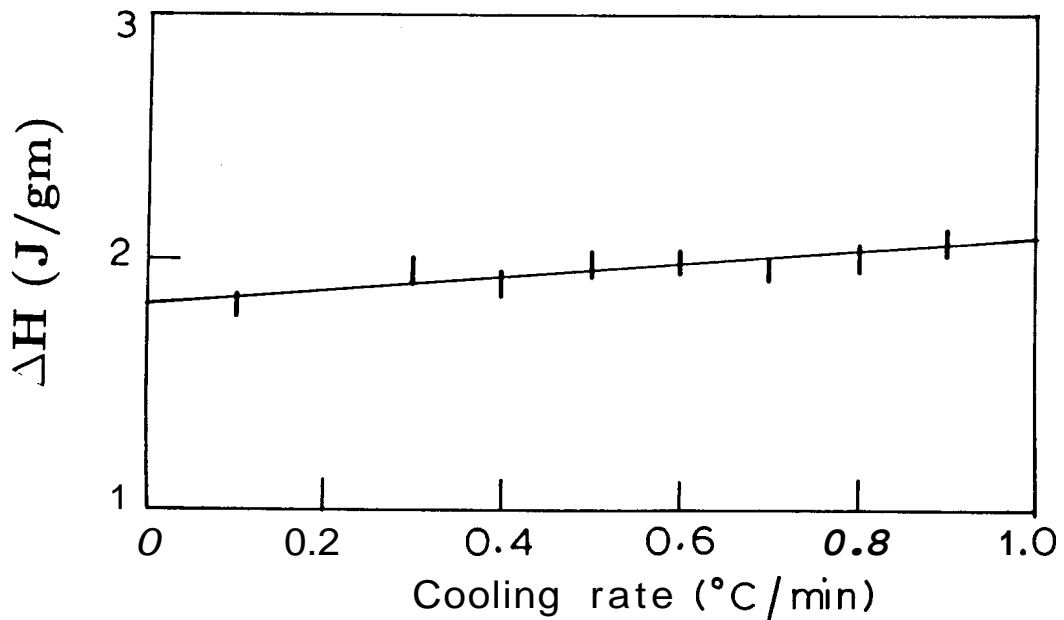


Figure 2.10: A plot of enthalpy (ΔH) versus cooling rate for the A-C* transition in MCP70B as obtained by the DSC runs. Each data point is represented by a vertical line the height of which represents the error bar in the determination of ΔH . The solid line is the least-square-fit of the data to a straight line.

strong peak for the A-C* transition. The DSC runs were taken for 10 different rates, ranging from 1°C/min. to 0.1°C/min., the lowest rate possible with our DSC set up. The total area under the endothermic peak was calculated using the computerised TADS system and the corresponding enthalpy (ΔH) was obtained for each cooling rate. The transition enthalpy includes both the latent heat and the specific heat contribution. In Figure 2.10 the value of ΔH thus obtained is plotted as a function of cooling rate and is fitted to a straight line. The zero intercept of this fitting gives the enthalpy ΔH_0 , the value that would be for a zero cooling rate. Although, in principle, DSC cannot differentiate between rapidly varying entropy and the latent heat of transition, earlier studies [14,15] have demonstrated that the value of ΔH , evaluated in this manner is very close to latent heat of transition. It is seen from the figure that ΔH is almost independent of the rate of cooling, which is as expected for first order transition with a small pretransitional effect. This gives a strong indication that the A - C* transition in MCP70B may be first order.

In order to establish this fact we have carried out high precision X-ray experiments. Figure 2.11 shows the raw diffractometer scans in the neighbourhood of the A-C* transition. It can be seen from the figure that both in the A and C* phases, we get single X-ray diffraction peak, whereas in the transition region, the diffraction pattern consists of wave vectors corresponding to both A and C* phases. Figures 2.12 and 2.13 show the temperature variation of the layer spacing (d) and the peak intensity of the X-ray diffraction peaks across the A-C* transition. From both the plots, it is seen that the width of the two-phase region is about 50 mK. The salient features of this two phase region are as follows.

Chapter 2: First order A-C / A-C* Transition

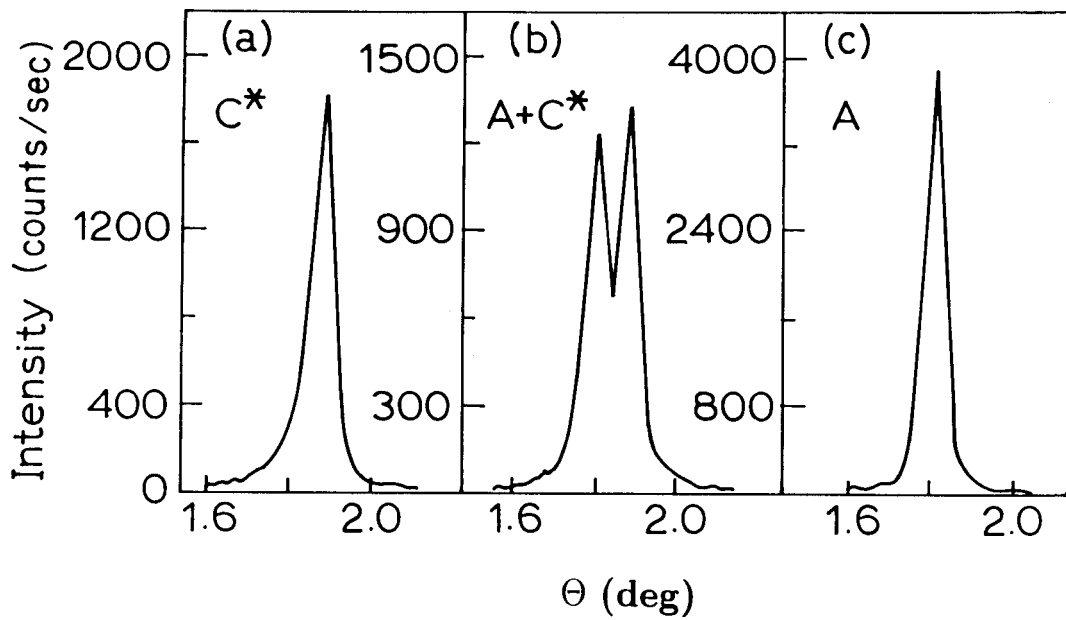


Figure 2.11: Raw diffractometer scans taken along the equatorial direction in the (a) C* phase (53.9°C), (b) two-phase region (54.0°C) and (c) A phase (54.0°C) of MCP70B. The coexistence of two density modulations in the two-phase region signifies that the A-C* transition is first order.

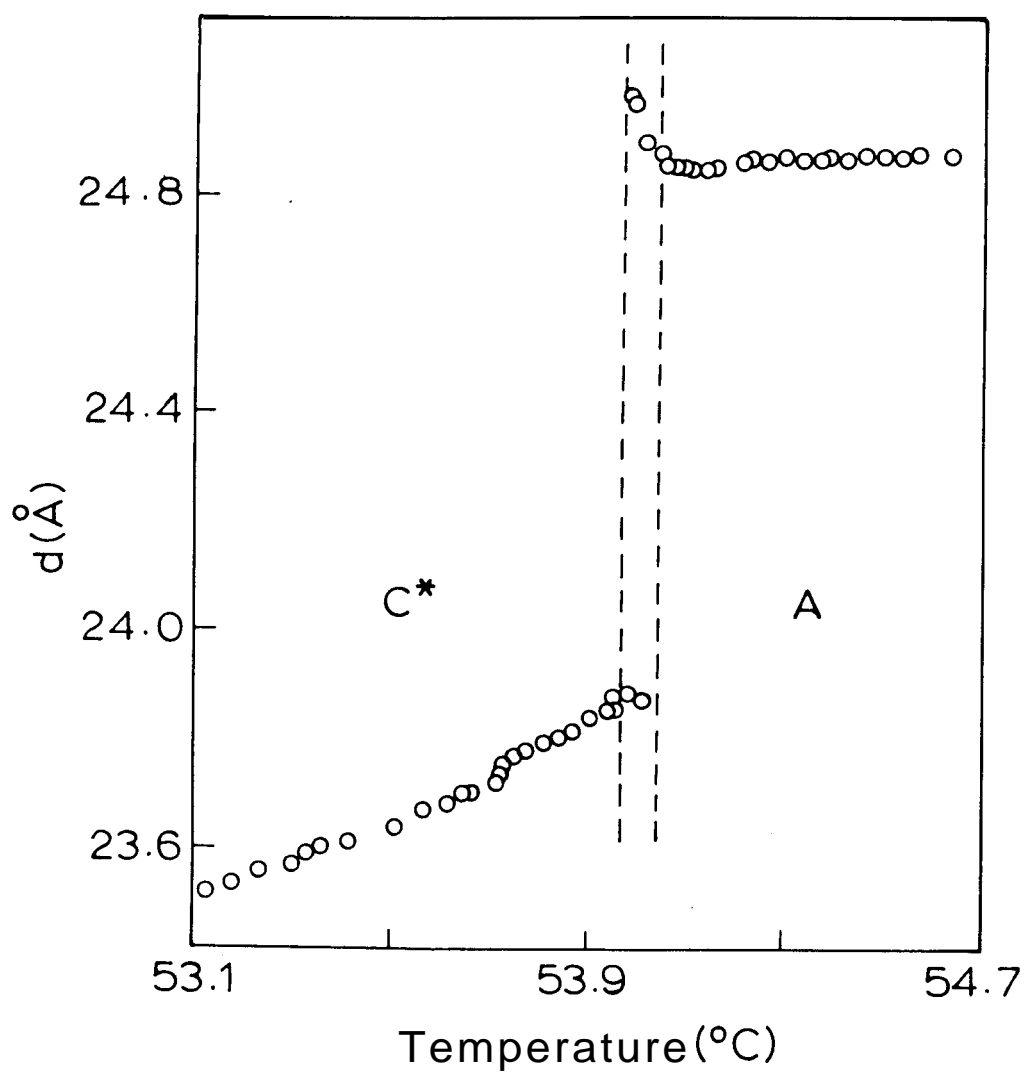


Figure 2.12: Variation of the smectic layer spacing (d) with temperature in the vicinity of the A-C* transition in MCP70B. The vertical dashed lines indicate the two-phase region.

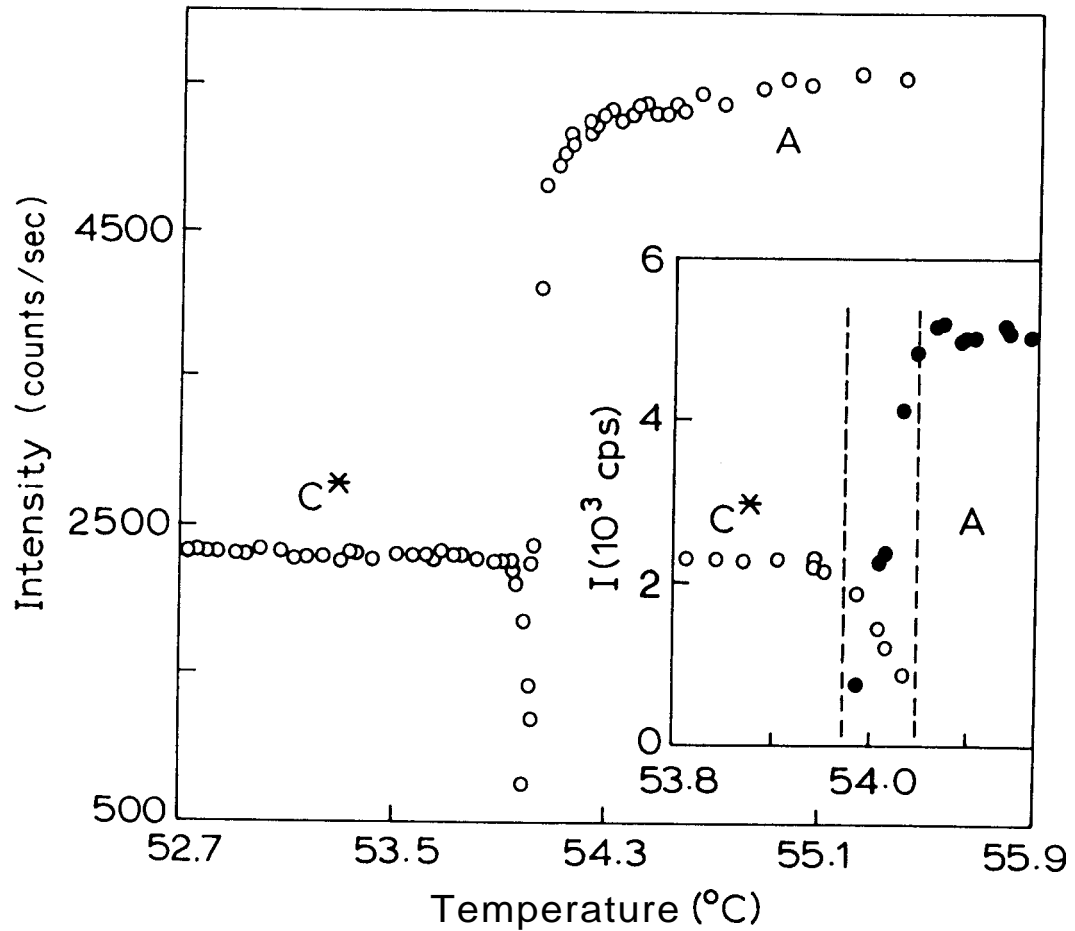


Figure 2.13: Variation of the intensity of the X-ray diffraction maxima as a function of temperature for MCP70B. The data in the immediate vicinity of the A-C* transition are shown on an enlarged scale in the inset. Solid and open circles in the inset correspond to the density modulations in the A and C* phases respectively. A crossover of the intensity is seen in the two phase region.

Chapter 2: First order A-C* / A-C Transition

1. The coexistence of peaks corresponding to both A and C* phases.
2. Cross-over of the intensities of X-ray diffraction peaks, occurring roughly in the mid position of the two-phase region.

These features are characteristic of a two-phase region which is expected and indeed seen for first order transitions between two smectic phases with different layer periodicities[16,17]. The tilt angle θ was calculated using the Equation 2.2. (d_A was taken as the layerspacing value in the A phase, just before the commencement of the two phase region.)

The validity of the above equation to calculate θ was verified by measuring the tilt angle directly from the 'four-spot' X-ray diffraction pattern in the C* phase. This was obtained using the X-ray photographic set up[18], where the sample was aligned in the presence of magnetic field and the molecules were held fixed by the field in the C* phase. The X-ray diffraction pattern taken on a photographic film consisted of "four-spots" as shown in Figure 2.14. The tilt angle (θ_p) (the subscript p indicates that the tilt angle was obtained from the photographic set up) was calculated directly by measuring the angle between the adjacent spots. The value of tilt angle obtained by the direct method and by Equation 2.2 are nearly the same, i.e., the ratio $\frac{\theta}{\theta_p} \simeq 1$. This clearly indicates that the molecules of MCP7OB are more like rigid-rods and are not in the Wulff limit[19]. Figure 2.15 shows the tilt angle data as a function of temperature. It is seen from the figure that the tilt angle values obtained by the two methods (open circle – from Equation 2.2, filled circle – four-spot method) agree quite well. The tilt angle θ shows a discontinuous jump at the transition. (As discussed

Chapter 2: First order A-C / A-C* Transition

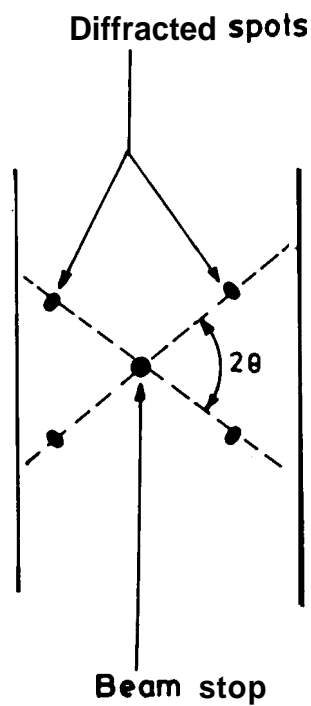
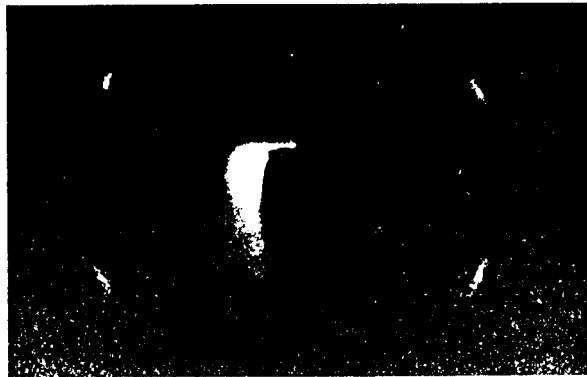


Figure 2.14: The 'four-spot' X-ray diffraction picture in the C* phase obtained from the photographic technique. The schematic is shown below.

Chapter 2: First order A-C / A-C* Transition

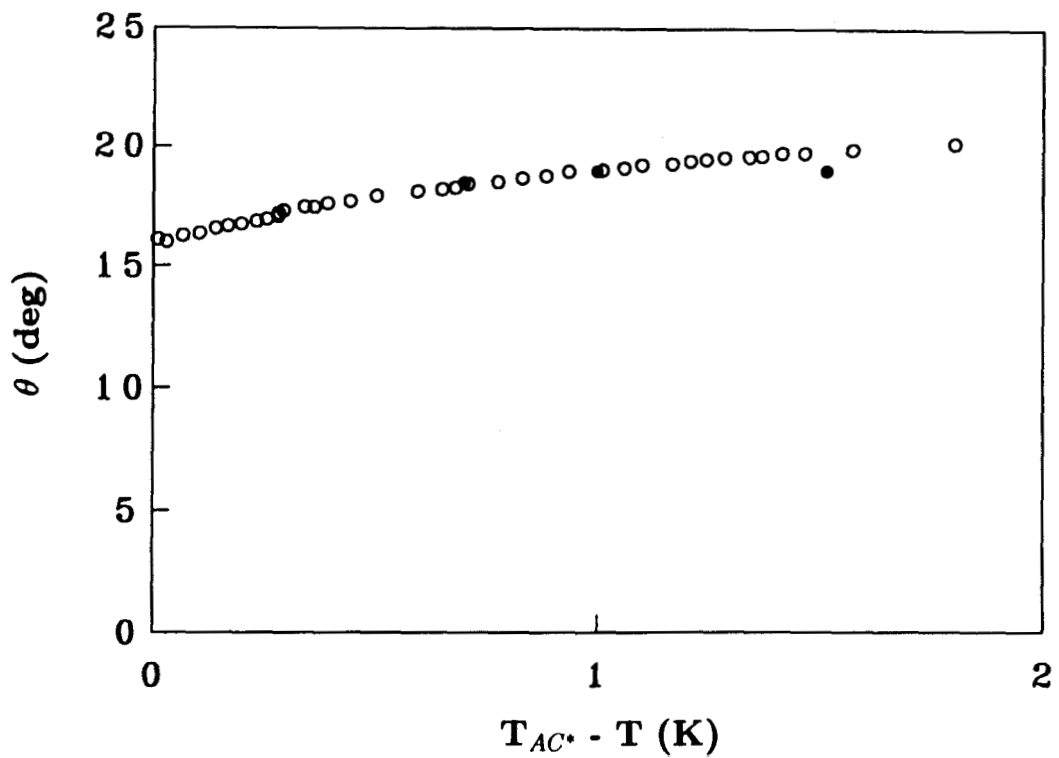


Figure 2.15: Variation of the tilt angle as a function of temperature for MCP70B. The open circles represent the data obtained using Equation 2.2. The filled circles are from the photographic experiments.

already, a discontinuous jump in the order parameter is characteristic of first order transition.) Thus we have a clear evidence of a first order A-C* transition in this ferroelectric material.

Having found a first order A-C* transition, it would be interesting to know what are the different material parameters that may drive this transition to become first order. Huang [20] has compiled all the available data on A-C/A-C* transitions in different compounds and found a systematic trend with respect to the temperature range of the A phase. The study indicated the possibility of finding a first order A-C/A-C* transition by shrinking the temperature range of the A phase. In a recent study, Liu et al[21] have argued that reducing temperature range of the A phase alone may not make the transition first order, but an additional parameter, viz., the magnitude of the transverse dipole moment of the constituent molecules has a strong effect on the order of the transition. A more systematic study in this direction was essential to understand the nature of this transition. With this in view, we have carried out X-ray experiments on two different liquid crystalline systems; one of which has the molecules with weak transverse dipole moment[22] (TBnA series) and another with a strong transverse dipole moment (A7[left-handed] or A7[l]). The structural formula and the transition temperatures of these materials are already given in Table 2.1.

In the TBnA series, the X-ray measurements were carried out on n=10 (TBDA), n=8(TBOA) and a 10% mixture of TBOA in TBDA. The PSD set up (explained in §2.2.4) was used for these experiments. Figure 2.16 shows the

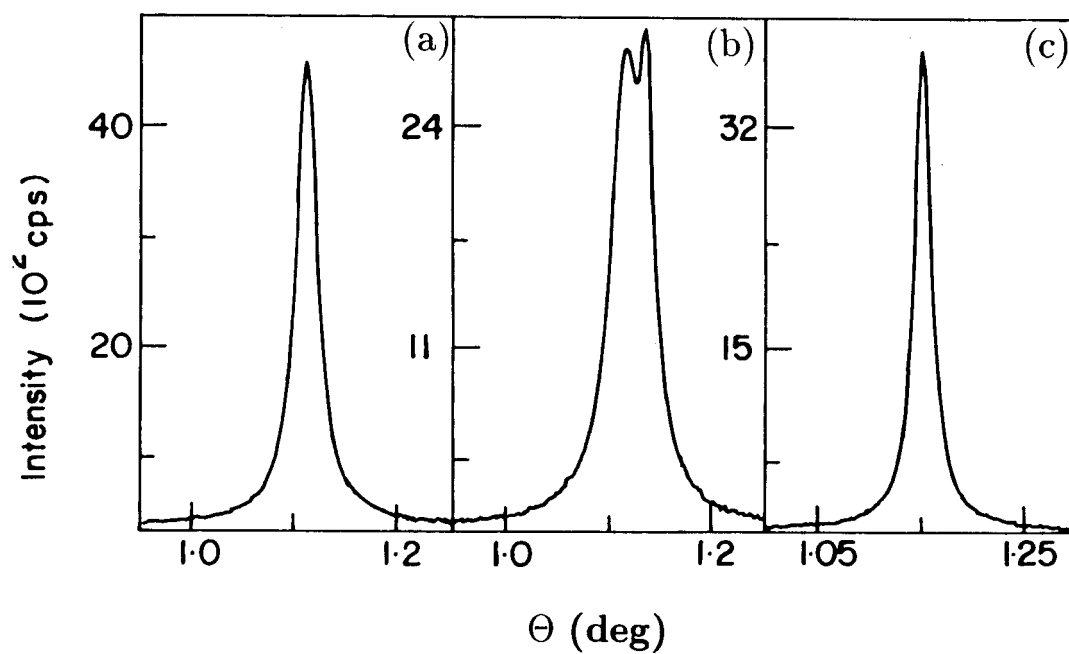


Figure 2.16: Raw PSD scans taken along the equatorial direction in the (a) A phase, (b) two-phase region and (c) C phases of TBDA.

PSD scans taken in the immediate proximity of the A-C transition in TBDA. The onset of the transition is characterized by the X-ray diffraction pattern consisting of two quasi Bragg peaks, at wave vectors corresponding to both A and C phases, signifying a two phase region. This is very similar to what was observed in the case of MCPSOB. The temperature variation of layer spacing (d) across the A-C transition is plotted in Figure 2.17. The figure shows the characteristic features of a first order transition, viz., the jump in the layer spacing (d) at the transition and existence of a two-phase region in which the d values corresponding to A and C phases coexist. Figure 2.18 shows the plot of θ , calculated using Equation 2.2, versus temperature. A discontinuous jump in θ shows that the A-C transition in TBDA is indeed a first order transition. Although earlier X-ray studies[23,24] had indicated the occurrence of a first order A-C transition in substances with weak transverse dipole moments, the data were not of sufficiently high resolution, - as the authors of Ref.[24] themselves point out- to yield any conclusive results. Thus we have observed a clear evidence of a first order A-C transition in such materials.

Having observed a first order A-C transition in TBDA with an A phase temperature range of $\sim 1.8^\circ\text{C}$, we proceeded to investigate whether the strength and order of this transition is affected merely by increasing the temperature range of the A phase without altering the basic structure of the constituent molecules. With this in mind, X-ray studies have been done on the lower homologue of the TBDA, viz., TBOA and a binary mixture of 10% TBOA in TBDA (molar concentration). The temperature range of the A phase for TBOA is $\sim 10^\circ\text{C}$ and for the mixture it is $\sim 2.9^\circ\text{C}$. The θ versus temperature data plots for TBDA,

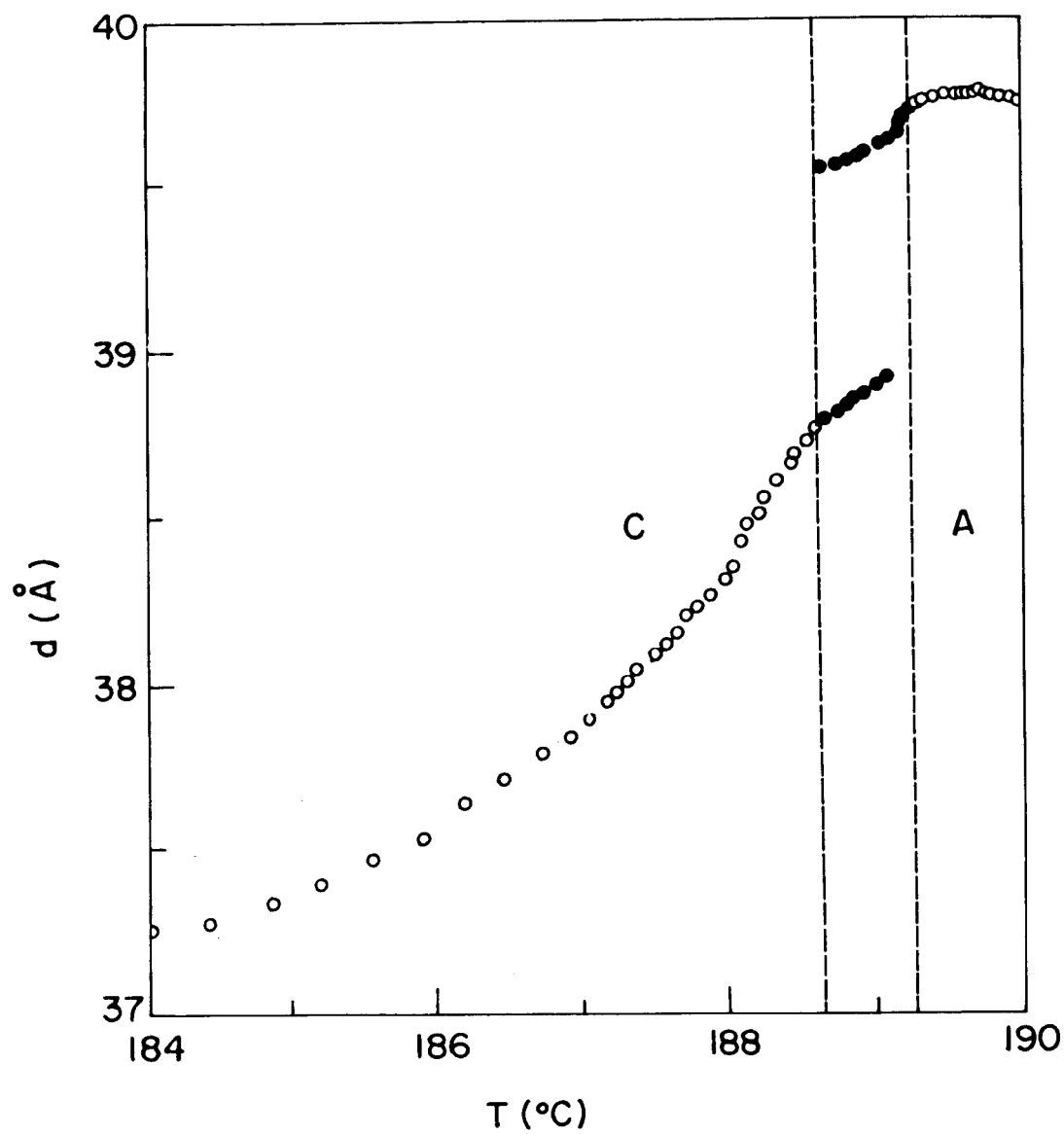


Figure 2.17: Temperature variation of the smectic layer spacing (d) in the vicinity of the A-C transition of TBDA. The dashed lines enclose the two-phase region.

Chapter 2: First order A-C / A-C* Transition

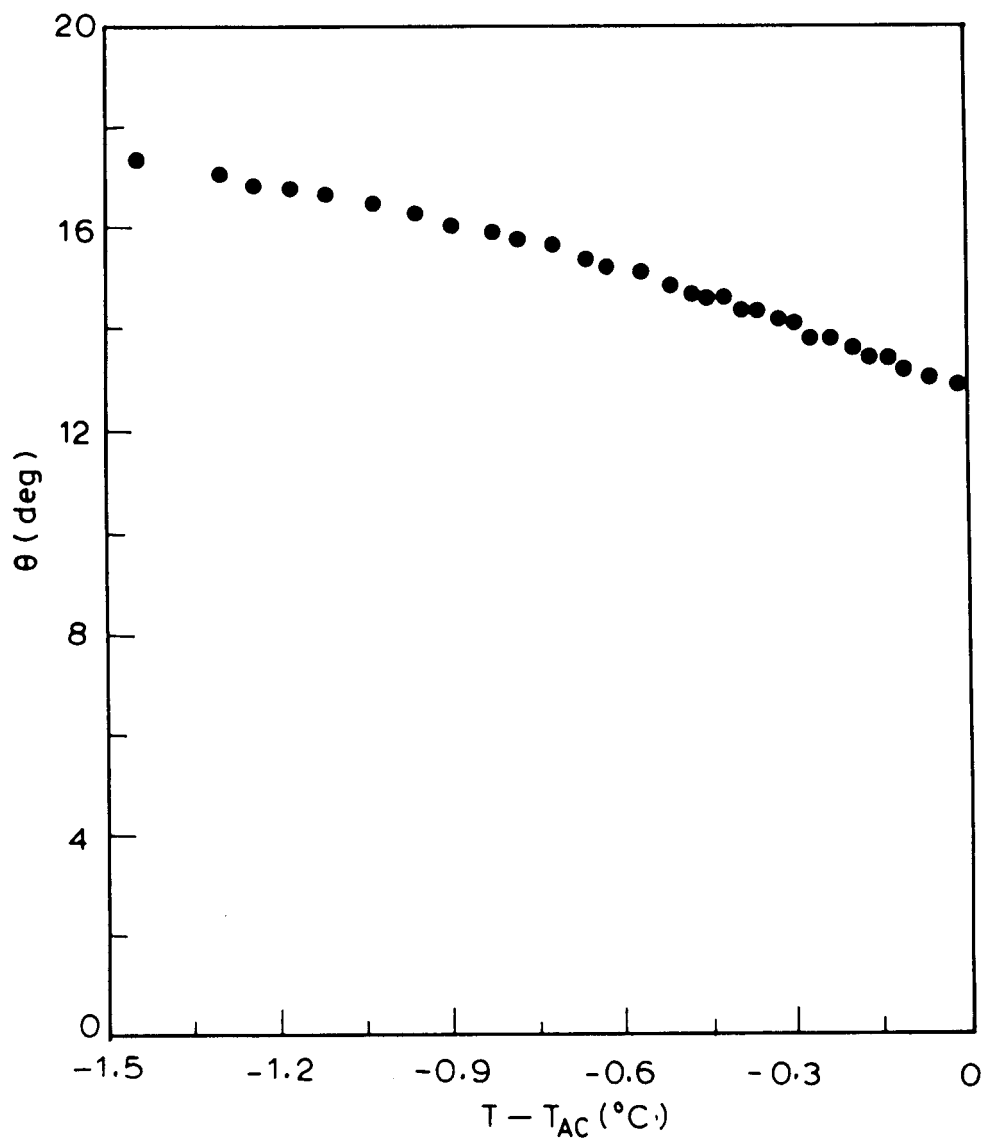


Figure 2.18: Temperature variation of tilt angle for TBDA.

TBOA and 10% mixture are shown in Figure 2.19. Table 2.4 gives the range of the A phase and the jump in θ at the transition for all the three materials. It is seen from the figure as well as from the Table that as the range of the A phase decreases, the order of the transition changes from second to first and increases in strength with further decrease in the range of A phase. Therefore, even though the materials have weak transverse dipole moment, the temperature range of the A phase determines the order of the transition.

X-ray measurements have also been carried out on A7(l), a left-handed chiral substance with a structural formula similar to that of MCPTOB (see Table 2.1). It has a high spontaneous polarisation (P , $\sim 150\text{nC/cm}^2$) indicating a strong transverse dipole moment. The temperature range of the A phase is relatively large ($\sim 8^\circ\text{C}$). Figure 2.20 shows the layerspacing (d) variation with temperature. The plot shows the existence of a two-phase region. Also plotted in the Figure 2.21 is the thermal variation of peak intensity which shows a cross-over in the two-phase region. The tilt angle θ as a function of temperature is plotted in Figure 2.22. It is seen from the figure that θ shows a discontinuous jump at the transition. These results are clearly indicative of a first order transition. High resolution calorimetric studies by Liu et al [25] have also shown that A-C* transition in this material is first order.

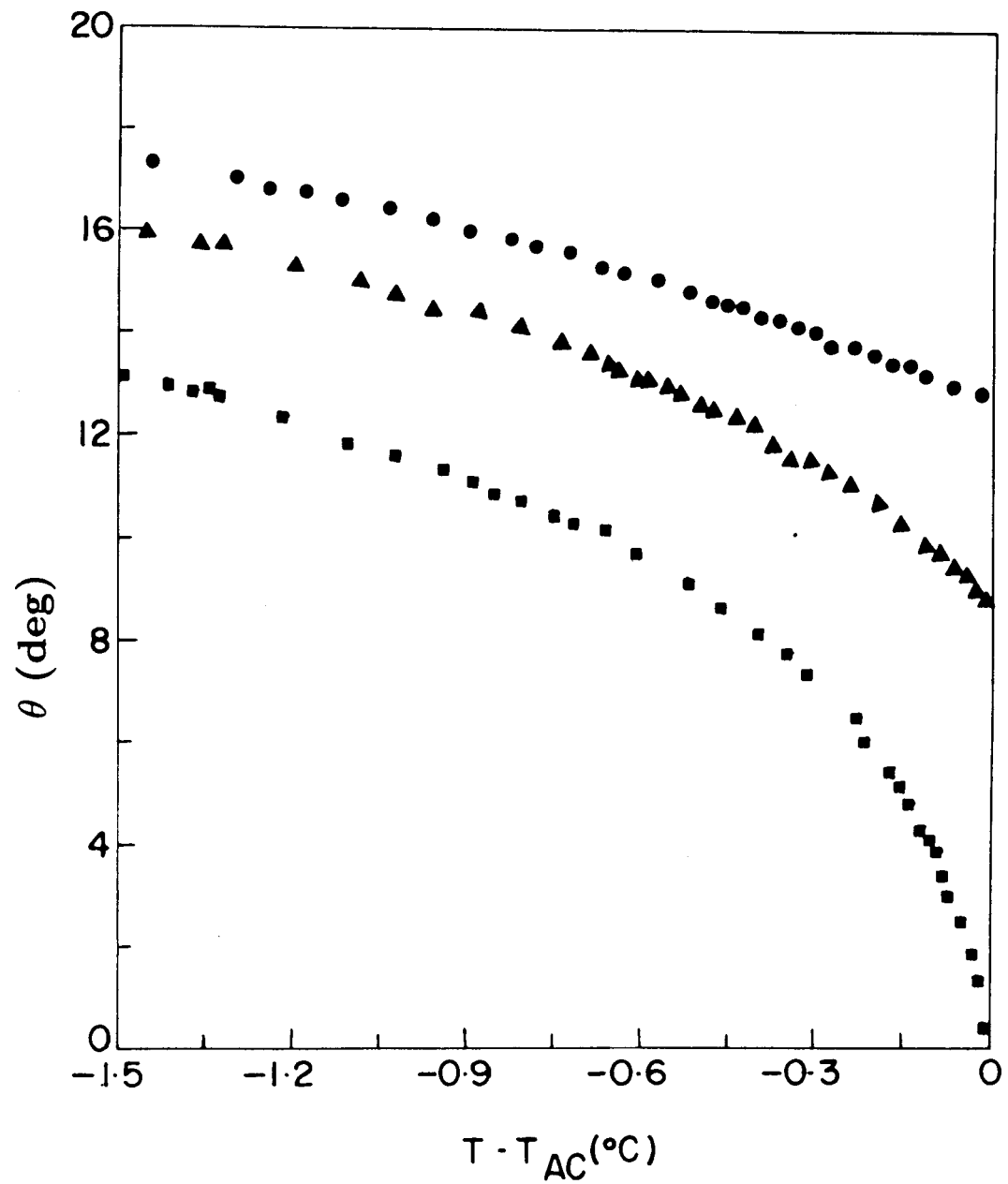


Figure 2.19: Thermal variation of the tilt angle for TBDA (circle), 10% TBOA + TBDA mixture (triangle), and TBOA (square).

Chapter 2: First order A-C* / A-C transition

Table 2.4: The temperature range of the A phase ($T_{I-A} - T_{A-C}$) and the jump in the tilt angle ($\Delta\theta$) at the A-C transition for the materials studied (where T_{I-A} is the isotropic - A transition temperature.)

Material	($T_{I-A} - T_{A-C}$) ($^{\circ}$ C)	$\Delta\theta$ (deg)
TBOA	10.0	0
10% TBOA + TBDA	2.9	8.9
TBDA	1.8	12.8

Chapter 2: First order A-C / A-C* Transition

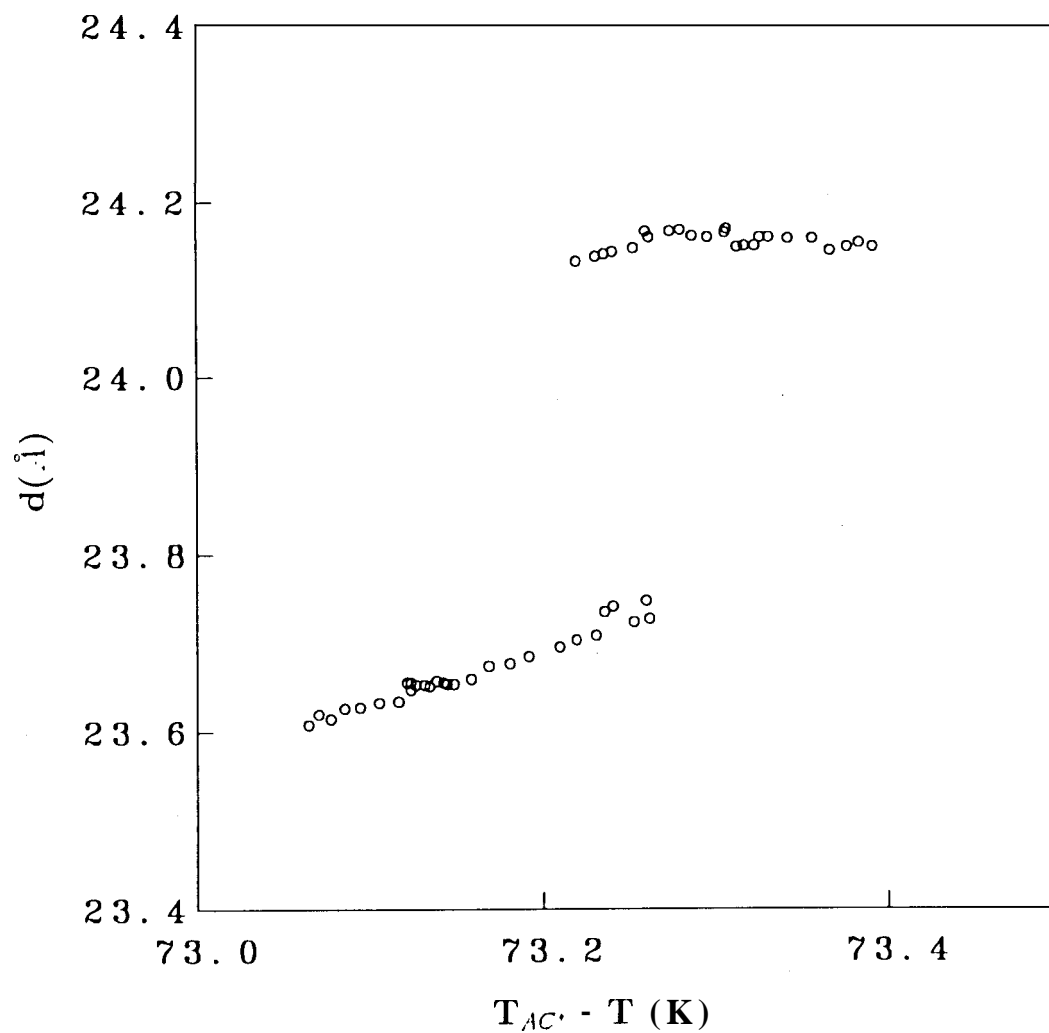


Figure 2.20: Temperature variation of the smectic layer spacing (d) in the close vicinity of the A-C* transition of A7(l).

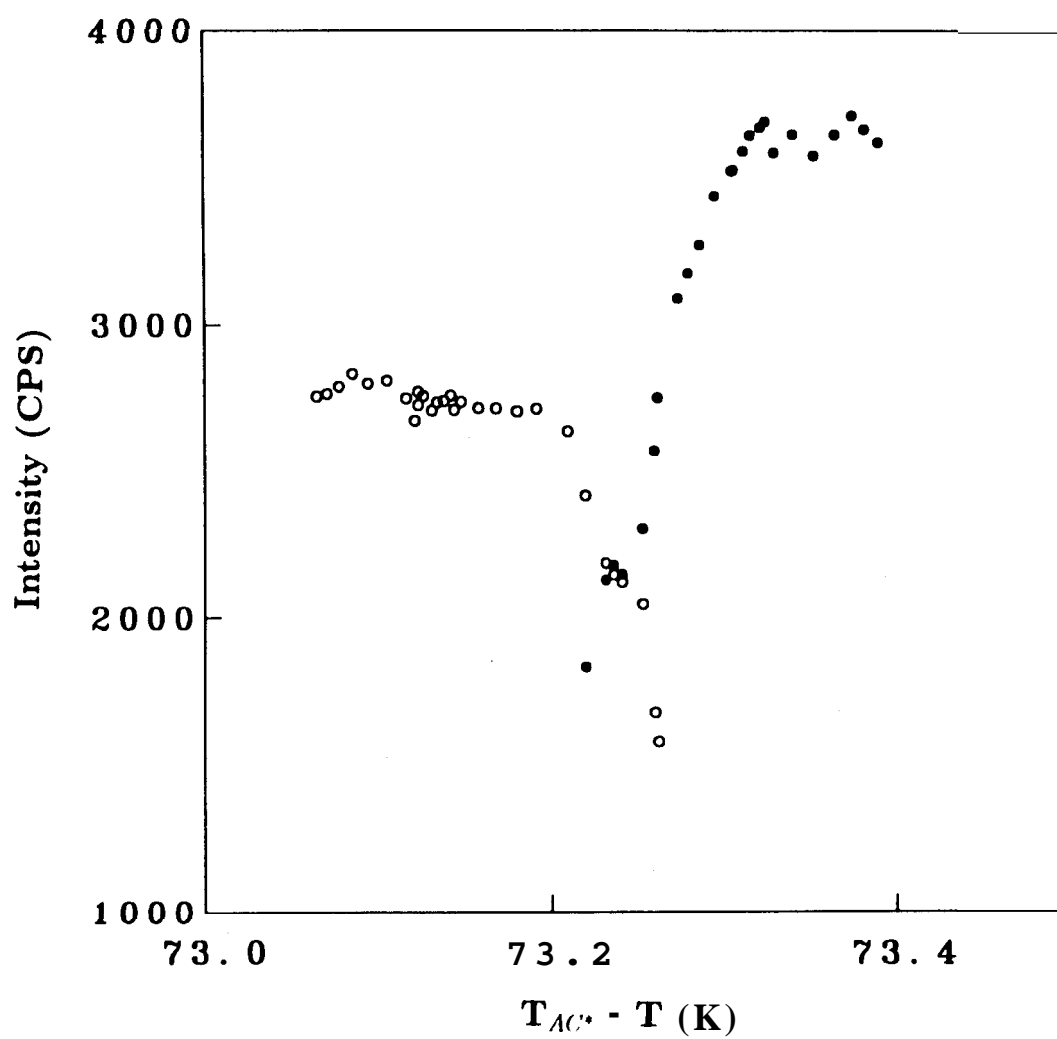


Figure 2.21: Variation of the peak intensity of the X-ray diffraction scans as a function of temperature near the A - C* transition of A7(l).

Chapter 2: First order A-C / A-C* Transition

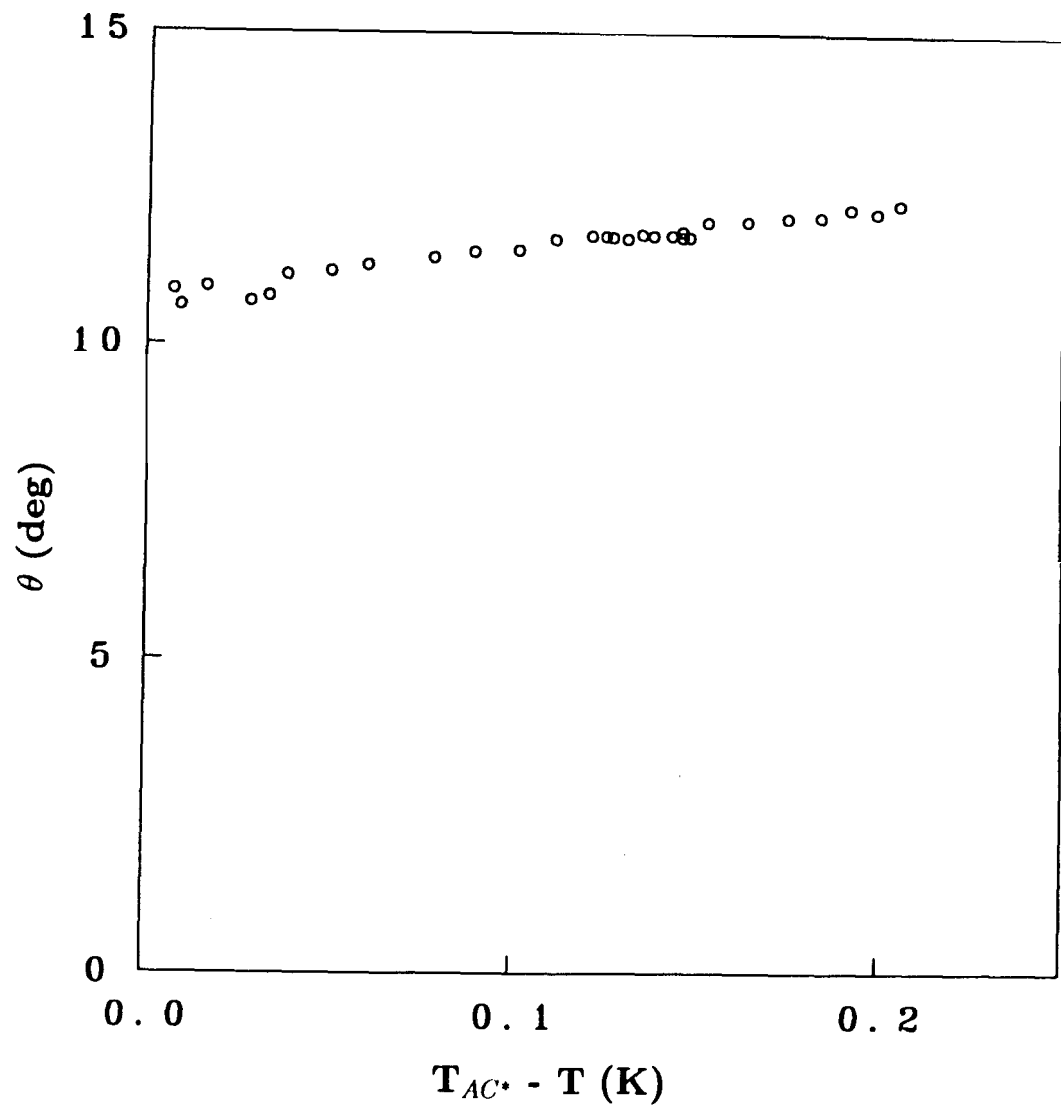


Figure 2.22: Variation of the tilt angle in the C* phase as a function of temperature for A7(l).

Based on the results discussed above, we can summarise the following about the nature of A-C/A-C* transition.

1. If the transverse dipole moment is strong, materials with a large range of A phase can show a first order A-C/A-C* transition.
2. For materials with weak transverse dipole moment the range of the A phase has to be much narrower for the same effect to be seen.

References

- [1] L. D. Landau and E. M. Lifshitz, *Statistical Physics*, Vol.5, Pergamon Press, Oxford (1980).
- [2] W. Helfrich and C. S. Oh, *Mol. Cryst. Liq. Cryst.* 14, 289 (1971).
- [3] R. B. Meyer, L. Liebert, L. Strzelecki and P. Keller, *J. Physique Lett.* **36**, L-69 (1975).
- [4] P. G. de Gennes, *Mol. Cryst. Liq. Cryst.* 21, 49 (1973).
- [5] S. C. Lien, C. C. Huang and J. W. Goodby, *Phys. Rev. A* 29, 1371 (1984).
See also R. B. Meyer, *Mol. Cryst. Liq. Cryst.* 40, 33 (1977).
- [6] S. C. Lien and C. C. Huang, *Phys. Rev. A* 30, 624 (1984).
- [7] Ch. Bahr and G. Heppke, *Mol. Cryst. Liq. Cryst. Lett.* 4, 31 (1986).
- [8] T. Sakurai, N. Mikani, R. Higuchi, M. Honma, M. Ozaki and IC. Yoshino, *J. Chem. Commun.* 978 (1986).
- [9] Ch. Bahr and G. Heppke, *Mol. Cryst. Liq. Cryst.* 148, 29 (1987).
- [10] S. Somashekara, *Experimental studies of phase diagrams of liquid crystals*, Ph.D. Thesis, University of Mysore, 1988.
- [11] V. Shubha and T. G. Ramesh, *J. Phys. E. (Sci. Instrum.)* 19, 916 (1986).
- [12] A. J. Leadbetter, J. C. Frost, J. P. Gaughan, G. W. Gray and A. Mosley, *J. de Physique* 40, 375(1979).

- [13] F. Hardouin, A. M. Levelut, J. J. Benattar and G. Sigaud, *Solid State Commun.* 33, 337 (1980).
- [14] B. R. Ratna and S. Chandrasekhar, *Mol. Cryst. Liq. Cryst.* , **162B**, 157 (1988).
- [15] V. N. Raja, R. Shashidhar, B. R. Ratna, G. Heppke and Ch. Bahr, *Phys Rev. A* 37, 303 (1988).
- [16] P. S. Pershan, G. Aeppli, J. D. Litster and R. J. Birgeneau, *Mol. Cryst. Liq. Cryst.* **67**, 205 (1981).
- [17] R. Shashidhar, B. R. Ratna, S. Krishna Prasad, S. Somasekhara and G. Heppke, *Phys. Rev. Lett.* 59,1209 (1987).
- [18] R. Shashidhar, K. A. Suresh, B. R. Ratna, S. Krishna Prasad, Ch. Bahr, A. Ostreicher and G. Heppke, *Mol. Cryst. Liq. Cryst.* 1, 89(1985).
- [19] A. Wulf, *Mol. Cryst. Liq. Cryst*, **56** 123 (1979).
- [20] See, eg., C. C. Huang, in *Theory and Applications of Liquid Crystals*, p. 185, edited by J. L. Ericksen and O. Kinderlehrer (Springer-Verlag, New York, 1987).
- [21] H. Y. Liu, C. C. Huang, T. Min, M. D. Wand, D. M. Walba, N. A. Clark, Ch. Bahr and G. Heppke, *Phys. Rev. A* 40, 6759 (1989).
- [22] L. Benguigui, *Liquid Crystals of One- and Two- dimensional order*, edited by W. Helfrich and G. Heppke (Springer-Verlag, New York, 1980) p.125

From the dielectric anisotropy measurements on TBBA, this author concludes that the transverse dipole moment of the molecule should be extremely small. It is reasonable to assume that the higher homologues TBOA and TBDA also have very weak transverse dipole moments.

- [23] S. Kumar, *Phys. Rev. A* **23**, 3207 (1981).
- [24] S. Diele, P. Schiller, A. Wiegeleben and D. Demus, *Cryst. Res. Technol.* **24**, 1051 (1989).
- [25] H. Y. Liu, C. C. Huang, Ch. Bahr and G. Heppke, *Phys. Rev. Lett.* **61**, 345 (1988).